*Nano Research* 2018, 11(3): 1358–1368
https://doi.org/10.1007/s12274-017-1750-9
**Research Article**
ISSN 1998-0124
CN 11-5974/O4

# Effects of redox-active interlayer anions on the oxygen evolution reactivity of NiFe-layered double hydroxide nanosheets

Daojin Zhou[1], Zhao Cai[1], Yongmin Bi[1], Weiliang Tian[1,2], Ma Luo[1], Qian Zhang[1], Qian Zhang[1], Qixian Xie[1], Jindi Wang[1], Yaping Li[1], Yun Kuang[1], Xue Duan[1], Michal Bajdich[3], Samira Siahrostami[4] (✉), and Xiaoming Sun[1] (✉)

[1] *State Key Laboratory of Chemical Resource Engineering, College of Energy, Beijing Advanced Innovation Center for Soft Matter Science and Engineering, Beijing University of Chemical Technology, Beijing 100029, China*
[2] *Key Laboratory of Chemical Engineering in South Xinjiang, College of Life Science, Tarim University, Alar 843300, China*
[3] *SUNCAT Center for Interface Science and Catalysis, SLAC National Accelerator Laboratory, Menlo Park, California 94025, USA*
[4] *SUNCAT Center for Interface Science and Catalysis, Department of Chemical Engineering, Stanford University, Stanford, California 94305, USA*

**Received:** 17 May 2017
**Revised:** 14 June 2017
**Accepted:** 23 June 2017



**KEYWORDS**
oxygen evolution reaction, layered double hydroxide, intercalated anions, electronic structure

## ABSTRACT

Nickel-iron layered double hydroxide (NiFe-LDH) nanosheets have shown optimal oxygen evolution reaction (OER) performance; however, the role of the intercalated ions in the OER activity remains unclear. In this work, we show that the activity of the NiFe-LDHs can be tailored by the intercalated anions with different redox potentials. The intercalation of anions with low redox potential (high reducing ability), such as hypophosphites, leads to NiFe-LDHs with low OER overpotential of 240 mV and a small Tafel slope of 36.9 mV/dec, whereas NiFe-LDHs intercalated with anions of high redox potential (low reducing ability), such as fluorion, show a high overpotential of 370 mV and a Tafel slope of 80.8 mV/dec. The OER activity shows a surprising linear correlation with the standard redox potential. Density functional theory calculations and X-ray photoelectron spectroscopy analysis indicate that the intercalated anions alter the electronic structure of metal atoms which exposed at the surface. Anions with low standard redox potential and strong reducing ability transfer more electrons to the hydroxide layers. This increases the electron density of the surface metal sites and stabilizes their high-valence states, whose formation is known as the critical step prior to the OER process.

## 1 Introduction

The oxygen evolution reaction (OER) plays an important role in many energy conversion systems such as electrolyzers and metal-air batteries [1–3]. The identification of highly efficient OER catalysts has

Address correspondence to Xiaoming Sun, sunxm@mail.buct.edu.cn; Samira Siahrostami, samiras@stanford.edu

been the subject of a considerable amount of research in recent years [4–24]. Although noble-metal oxides (e.g., $IrO_2$ and $RuO_2$) and their transition metal-doped counterparts are the state-of-the-art OER electrocatalysts, large-scale practical applications of these compounds are severely limited by their limited availability, high cost, and poor stability [25, 26].

Among different reported OER catalysts, NiFe-layered double hydroxides (NiFe-LDHs) with highly tunable compositions and structures represent a promising alternative as OER catalysts in basic solutions, owing to their outstanding performance and lower costs compared to noble-metal oxides [9, 27–30]. The recent improved understanding of the nature of LDH-based materials has led to the design and synthesis of related high-performance catalysts [31–34]. The Ni:Fe ratio has been demonstrated to significantly affect the OER activity of these materials [35–37]. For a given Ni:Fe ratio, a smaller size and a lower crystallinity are believed to be beneficial for the OER performance of LDHs, by exposing a larger number of active sites [27, 38, 39]. Moreover, it has been reported that the exfoliation and exposure of specific lattice planes also influence the OER performance of the NiFe-LDHs [29, 40–42]. These previous reports mainly focused on the laminate composition, crystallinity, and exfoliation degree of the NiFe-LDHs. Only few studies focused on the introduction of intercalated anions in the LDHs laminates; this process has the potential to modify the electron density of metal sites in the laminates and ultimately provide a new route for tuning the OER performance of the NiFe-LDHs [43, 44]. A recent study by Müller et al [44] showed that the OER activity of the NiFe-LDHs increases with the basicity of the intercalated anions such as $BF_4^-$, $Cl^-$, $SO_4^{2-}$, and so on.

In this study, we seek to find a universal relationship between the standard redox potential of 16 different anion-intercalated NiFe-LDHs and their OER catalytic activity. Anion-intercalated NiFe-LDHs were prepared by a co-precipitation process, and the OER performance of the as-prepared materials was tested. The results highlight a correlation between the OER activity of the NiFe-LDHs and the redox potential of the intercalated anions, which suggests that anions with different reducing ability can be used to modify the electron density of surface metal sites in NiFe-LDHs. We confirmed this possibility by detailed electrochemical and X-ray photoelectron spectroscopy (XPS) characterizations combined with density functional theory (DFT) calculations, and attributed the enhanced OER activity of the intercalated compounds to the electron donation from the reducing anions to the laminates. This study provides a suitable route for the future design of catalysts with high OER efficiency.

## 2 Results and discussion

### 2.1 X-ray diffraction (XRD) analysis

The XRD patterns of NiFe-LDHs intercalated with different anions were collected and used to determine their crystalline phases and basal spacings using Bragg's law (Fig. 1).

As shown in Figs. 1(a)–1(d), all as-prepared NiFe-LDHs present the characteristic diffraction peaks of layered double hydroxides, which indicates that these NiFe-LDHs have similar structures. The $2\theta$ value of the (003) reflection ranges from 10.6° to 11.5°, corresponding to basal spacings of the NiFe-LDHs structures between 0.85 and 0.76 nm. Taking the phosphorus oxoanion-intercalated NiFe-LDHs as reference (Fig. 1(d)), the basal spacing increases from 0.79 nm for NiFe-($H_2PO_2^-$)-LDHs to 0.81 nm for NiFe-($HPO_3^{2-}$)-LDHs, reflecting the increasing anion radius from $H_2PO_2^-$ to $HPO_3^{2-}$ [45]. Similar results are also observed in Figs. 1(a)–1(c), in which the basal spacing of the NiFe-LDHs shows a positive correlation with the radius of the intercalated anions in the chlorine oxoanion, sulfur oxoanion, and halogen series. The larger basal spacing compared with the counterpart NiFe-($CO_3^{2-}$)-based LDHs [44] also indicates the successful intercalation of the anions in the NiFe-LDH interlayer. In addition, the diffraction peaks around 35° and 60° in the XRD patterns originate from the in-plane (100) and (110) reflections of the NiFe-LDHs and further confirm the formation of two-dimensional LDH nanosheets.

### 2.2 Fourier-transform infrared (FTIR) spectra

Based on the XRD results discussed above, FTIR spectra was collected to investigate the identity of the interlayer anions in the NiFe-LDHs (Fig. 2).

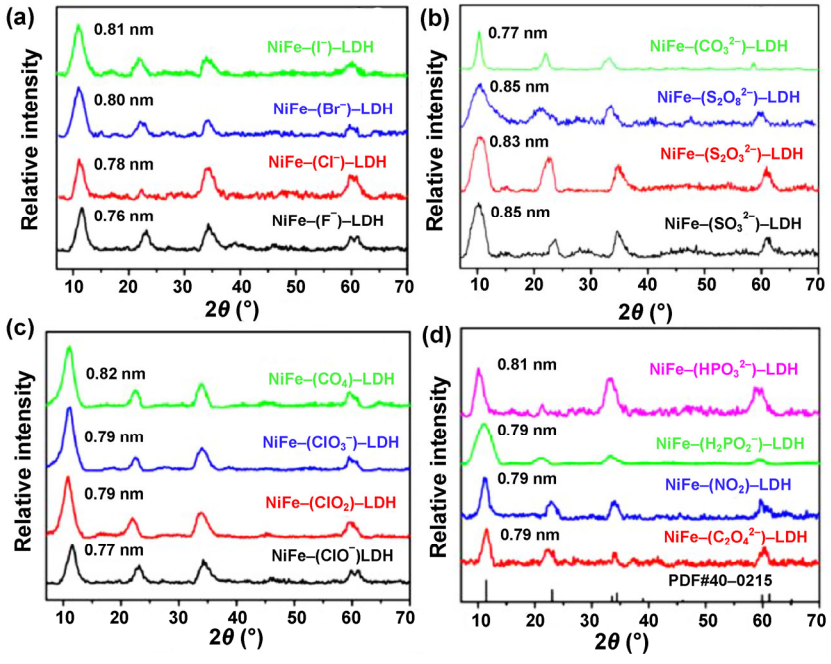


**Figure 1** XRD patterns of NiFe-LDHs intercalated with (a) halogens, (b) sulfur oxoanions and carbonates, (c) chlorine oxoanions, and (d) phosphorus oxoanions and C- or N-containing oxoanions, highlighting the similarity of their crystal structures.

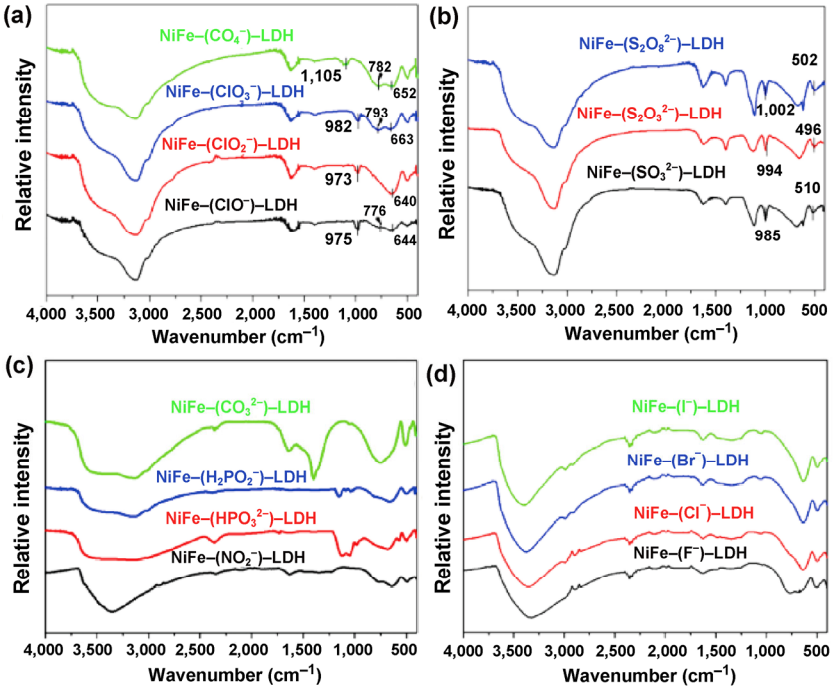


**Figure 2** Fourier-transform infrared spectra of LDHs intercalated with (a) chlorine oxoanions, (b) sulfur oxoanions, (c) phosphorus oxoanions or nitrites, and (d) halogens.

The FTIR spectrum of anion-intercalated LDHs is compared in Figs. 2(a)–2(d). The bands at 1,228 and 652 $cm^{-1}$ were assigned to the Cl–O stretching modes of $ClO_4^-$. The absorption bands ranging from 982 to 973 $cm^{-1}$ indicate the presence of Cl–O bonds in three other NiFe-($ClO^-$)-LDHs, NiFe-($ClO_2^-$)-LDHs and NiFe-($ClO_3^-$)-LDHs [46]. The characteristic S–O absorption bands are found between 1,002 and 985 $cm^{-1}$ (Fig. 2(b)).

[47] The S–S absorption band is located in the fingerprint region at 512 $cm^{-1}$. The peak corresponding to the symmetric P–O stretching is found around 1,054 and 1,041 $cm^{-1}$ for NiFe-($H_2PO_2^-$)-LDH and NiFe-($HPO_3^{2-}$)-LDH, respectively. The different positions of the absorption band for the same bond may be attributed to the different structure and interaction of the intercalated anions with the NiFe-LDH laminates. Compared with the FTIR spectrum of NiFe-($CO_3^{2-}$)-LDH in Fig. 2(c), the stretching vibration of alkali carbonates around 1,400 $cm^{-1}$ [48] was negligible in the other NiFe-LDHs. An appropriate pretreatment can effectively prevent intercalation of $CO_3^{2-}$ in the interlayer of NiFe-LDHs, whereas the FTIR characterization confirms the presence of all other anions in the corresponding NiFe-LDHs The combination of the present FTIR results with the XRD analysis reported in the previous section confirms the successful preparation of NiFe-LDHs intercalated by different anions.

### 2.3 Morphology measurements

The morphology of the prepared NiFe-LDHs was characterized by transmission electron microscopy (TEM), and the results (Fig. 3 and Figs. S1–S3 in the Electronic Supplementary Material (ESM)) highlight the nanosheet structure of each NiFe-(X)-LDH sample, where X stands for each different intercalated anion, respectively.

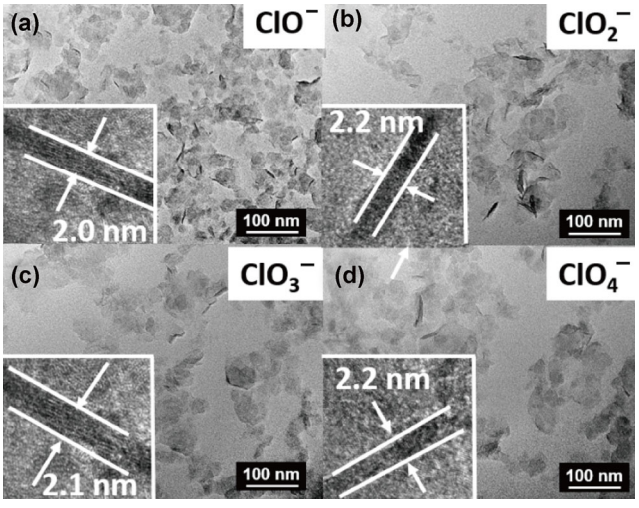


**Figure 3** TEM images of chlorine oxoanion-intercalated LDHs, showing similar size and crystallinity. The insets show the thickness of the corresponding LDHs.

All present LDHs have similar morphology and extent of exfoliation, and a size distribution approximately 50 nm wide, as shown in Fig. 3 and Figs. S1–S3 in the ESM. Taking into account the XRD results presented in Section 2.1 and the TEM data of this section, we conclude that the crystallinity, thickness, and size of the as-prepared LDHs have a negligible effect on their OER performances.

Furthermore, the composition of the LDH samples was accurately measured. Based on the stoichiometry data in Table S1 in the ESM, we can infer that the anionic content is close to 25% of the total metal amount, with a standard deviation of less than 20%; therefore, the effect of the amount of intercalated anions on the performances of the LDHs can also be considered negligible.

### 2.4 Electrocatalytic OER activity

The electrocatalytic OER activity of the prepared NiFe-LDHs was further characterized, and the corresponding polarization curves and Tafel plots are shown in Fig. 4 and Fig. S4 in the ESM.

The electrocatalytic OER activity of the as-prepared LDHs materials was investigated in alkaline solutions (0.1 M KOH), using a standard three-electrode system. In each series of NiFe-(X)-LDHs materials (intercalated with chlorine oxoanions, sulfur oxoanions, phosphorus oxoanions, and halogens), we observed a gradual increase in the onset potential with increasing redox potential of the anions. For example, the onset potentials in the chlorine oxoanion series, NiFe-($ClO^-$)-LDHs, NiFe-($ClO_2^-$)-LDHs, NiFe-($ClO_3^-$)-LDH, and NiFe-($ClO_4^-$)-LDH, are 1.51, 1.53, 1.55, and 1.55 V, respectively. A similar pattern is observed for other NiFe-LDHs (such as the sulfur oxoanion- and halogen-intercalated series). Among all materials examined, the NiFe-($H_2PO_2^-$)-LDHs show the lowest onset potential (1.45 V) and a current density decay < 10% after a 34,000 s test (inset of Fig. 4(d)). The onset potential of the NiFe-LDHs at 1 mA/$cm^2$ is plotted in Fig. 5(a) as a function of the standard redox potential (representative of the reducing ability) for each anion. Figure 5(a) clearly reveals a linear relationship between the onset potential of the NiFe-LDHs and the standard redox potentials of the intercalated anion (see Table S2 in the ESM for the corresponding half reactions) [49, 50].

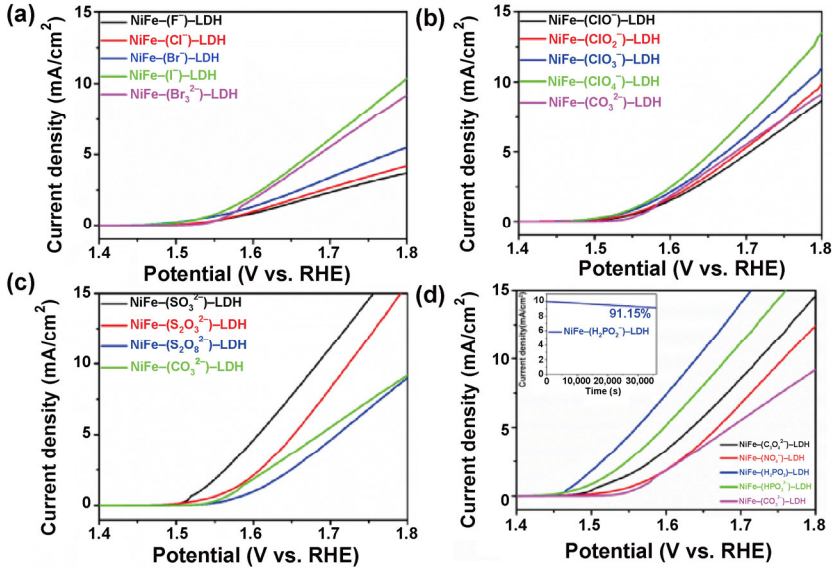


**Figure 4** Polarization curves of NiFe-LDHs intercalated with (a) halogens, (b) sulfur oxoanions, (c) chlorine oxoanions, and (d) phosphorus oxoanions and C- or N-containing oxoanions, showing the different OER activity of these compounds. The inset in (d) shows the time evolution of the current density of the NiFe-($H_2PO_2^-$)-LDHs.

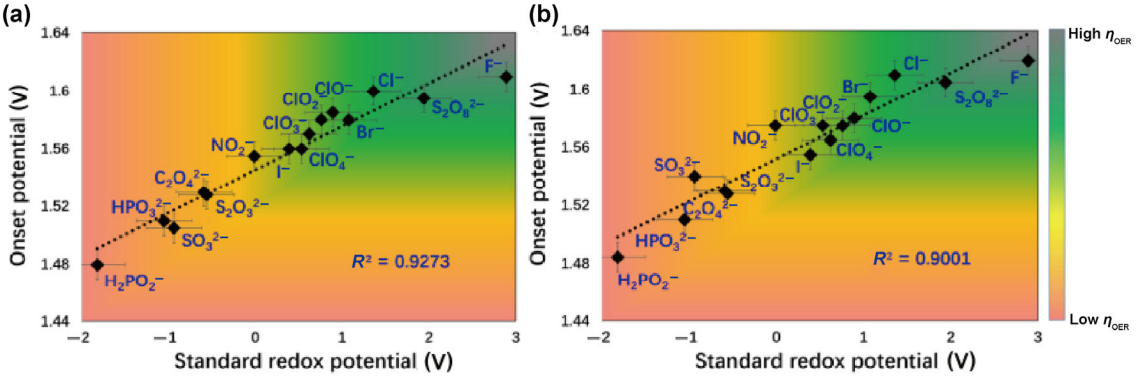


**Figure 5** Relationship between (a) onset potential and (b) capacitance-corrected onset potential measured at 1 mA/cm$^2$ with the standard redox potential of the examined anions.

As mentioned above, the three main factors affecting the intrinsic OER activity of the NiFe-LDHs are the Ni:Fe metal ions ratio, the crystallinity of the NiFe-LDHs, and the electron density on the metal sites in the NiFe-LDH laminates. We showed above that the Ni:Fe metal ions ratio, size, and crystallinity of the as-prepared NiFe-LDHs are similar regardless of the specific intercalated anions. In addition, we measured the electrochemical double-layer capacitance ($C_{dl}$) of each NiFe-LDH to expose differences in the electrochemical surface area (ECSA) [51]. Two methods have been proposed to determine the $C_{dl}$ of a catalyst: Cyclic voltammetry and AC impedance spectroscopy [52–54]. Since metal oxides or hydroxides are less electroconductive and have a potential-dependent conductivity [52], we added sufficient amounts of conductive carbon in the inks to ensure that their $C_{dl}$ could be accurately determined by cyclic voltammetry. The samples tested in this study show suitable conductivity even in the uncharged state. We further measured the $C_{dl}$ of a glassy carbon (GC) electrode by cyclic voltammetry (25 μF/cm$^2$), which was subtracted from the $C_{dl}$ of the NiFe-LDHs sample (~ 2,000 μF/cm$^2$). The huge difference between the $C_{dl}$ values of bare electrode and NiFe-LDHs samples illustrates that the obtained $C_{dl}$ of NiFe-LDHs is credible. The results in Figs. S5–S10 and Table S3 in the ESM show that the $C_{dl}$ values of the NiFe-LDHs differ by only ±15%. The

relationship between the capacitance-corrected onset potentials measured at 1 mA/cm$^2$ and the standard redox potentials of the examined anions, plotted in Fig. 5(b), shows a similar trend to the plot in Fig. 5(a). The correlation coefficients of the linear fits in Figs. 5(a) and 5(b) are 0.9273 and 0.9001, respectively. Excluding the effect of the crystallinity and ECSA of the NiFe-LDHs, these results indicate that the OER activity of the NiFe-LDHs depends on the reducing ability of intercalated anions. The Tafel slopes follow the same trend. In particular, the slopes measured for NiFe-($ClO^-$)-LDHs, NiFe-($ClO_2^-$)-LDHs, NiFe-($ClO_3^-$)-LDH, and NiFe-($ClO_4^-$)-LDH (Fig. S4 in the ESM) are 51.7, 60.9, 66.7, and 67.9 mV/dec, respectively. The relationship between the onset potential measured by the Tafel plots and the standard redox potential of the examined anions (Fig. S11 in the ESM) further confirms the observed trend. Müller et al. [44] showed that the OER performances of NiFe-LDHs are linked to the p*K*a of the conjugate acid of the intercalated anions; however, in our case we found that while HF and $HNO_2$ have similar p*K*a values (3.18 and 3.29, respectively), the OER performances of NiFe-($F^-$)-LDH and NiFe-($NO_2^-$)-LDH are significantly different (over 50 mV), suggesting a different relationship between the intercalated anions and the OER performance of the corresponding LDHs.

It is well known that the electronic structure of metal atoms (especially high-valence metals) exposed at the surface plays a critical role in the OER activity [55, 56]. The different OER activities observed for the present NiFe-LDHs might originate from the difference in the electron density of the metal sites in the NiFe-LDHs laminates, especially the difference in the stability of high-valence states, which is modified by the intercalated anions. Figure 6 illustrates the OER mechanism (Eqs. (1)–(4), where M stands for the catalytically active sites) of the NiFe-LDHs.

$$M + H_2O \longrightarrow M\text{-}OH + (H^+ + e^-) \quad (1)$$

$$M\text{-}OH \longrightarrow M\text{-}O + (H^+ + e^-) \quad (2)$$

$$M\text{-}O + H_2O \longrightarrow M\text{-}OOH + (H^+ + e^-) \quad (3)$$

$$M\text{-}OOH \longrightarrow M + O_2 + (H^+ + e^-) \quad (4)$$

Equations (1)–(4) show that the OER process involves stepwise deprotonation steps (Eqs. (2) and (4)), which also represent the high-activation energy or speed-limiting steps [57, 58]. As the deprotonation proceeded, higher-valence M states were formed (or maintained). Therefore, an environment that can help to protect or maintain high-valence states would be beneficial for lowering the activation energy and decreasing the overpotential. In other words, increasing the electrons shielding effect of the metal sites in LDHs would lead to a lower initial valence of the M site, and to more stable high-valence M states when charged, and consequently to an enhancement in the OER performance [59, 60]: This is the basic principle behind the activity of the intercalated anions. The introduction of anions with stronger reducing ability led to more electrons being transferred to the surface metal atoms, stabilizing their high-valence states and increasing the OER activity [59, 61].

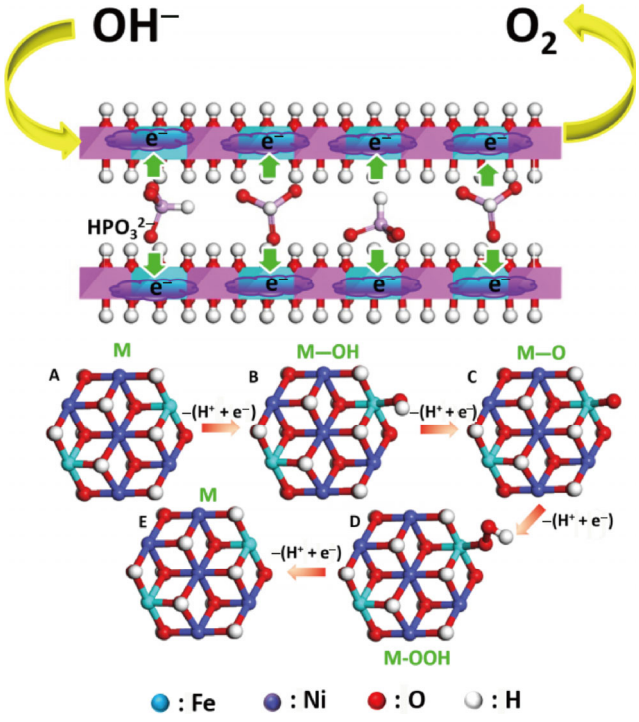


**Figure 6** Scheme of OER processes on NiFe-LDHs.

Using phosphate-intercalated LDH as an example (also in upper part of Fig. 6), electron transfer from phosphite to the Ni or Fe metals takes place prior to the OER and alters the electron density of the metals, leading to the formation of electron-rich metal sites. These electron-rich metals could then be easily oxidized to higher-valence states in the OER process, reducing the $\Delta G_{OOH}$ (Gibbs free energy of –OOH) of Eq. (3), and

the easily formed higher-valence metal centers can then act as active sites of $Ni_{1-x}Fe_xOOH$ [62]. By transferring more electrons to Fe, the onset potential of NiFe-($HPO_3^{2-}$)-LDH is lowered and its OER performance is improved.

Moreover, the potentiostatic stability tests of the as-prepared NiFe-LDHs in Fig. S12 in the ESM show that the more active catalysts also present acceptable stability. The current density drop is mainly attributed to the loss of active material during the release of $O_2$ bubbles. The intercalated anions were not replaced by $OH^-$ or oxidized, but steadily stored in the interlayer, which is consistent with previous observations [45] and Table S4 in the ESM. We selected NiFe-($SO_3^{2-}$)-LDH as a representative example of LDHs intercalated by anions with strong reducing ability. No significant changes in the elemental composition of NiFe-($SO_3^{2-}$)-LDH before and after the OER process were revealed by inductively coupled plasma (ICP) emission spectra. This finding was further confirmed using XPS measurements and DFT calculations.

### 2.5 XPS measurements

XPS analysis was used to investigate the effect of anions with different redox potentials on the electron density of the metal sites in the LDHs. We measured the difference between the electron density on the original metal sites in the as-prepared NiFe-($CO_3^{2-}$)-LDHs and on the metal sites in the materials intercalated with different anions. The non-metal atom content in the as-prepared NiFe-LDHs materials is quantitatively summarized in Table S1 in the ESM.

The Ni 2p and Fe 2p XPS spectra of NiFe-LDHs intercalated with different anions are displayed in Fig. 7, and Figs. S13 and S14 in the ESM. In the case of the sulfur oxoanion-intercalated NiFe-LDHs, the Ni $2p_{3/2}$ binding energy is shifted from 855.95 eV for NiFe-($SO_3^{2-}$)-LDH to 856.05 and 856.5 eV for NiFe-($S_2O_3^{2-}$)-LDH and NiFe-($S_2O_8^{2-}$)-LDH, respectively. This means that, as the reducing ability increases from $S_2O_8^{2-}$ to $SO_3^{2-}$, a much higher amount of charge is transferred from the intercalated anions to Ni, leading to a negative shift of the Ni $2p_{3/2}$ level and to a lower Ni valence state. The valence states of the Fe sites in sulfur oxoanion-intercalated NiFe-LDHs are illustrated in Fig. 7(b). The Fe sites show similar trends to the Ni

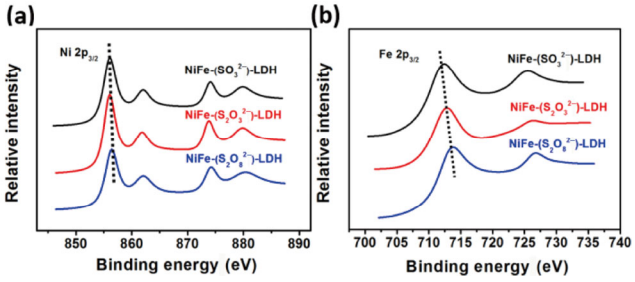


**Figure 7** XPS curves of Ni and Fe in sulfur oxoanion-intercalated NiFe-LDHs.

ones. The intercalation of anions with higher reducing ability in the interlayer of the NiFe-LDHs reduced the Fe valence in the corresponding sites. These results suggest that the intercalated anions significantly modify the electron density of the metal sites by inducing different amounts of transferred charge, and thus alter the OER activity of the corresponding NiFe-LDHs. Similar trends can also be found for the NiFe-LDHs intercalated with halogens, chlorine oxoanions, phosphorus oxoanions, and other anions (Figs. S13 and S14 in the ESM). In addition, the Ni, Fe, and S electronic structures of NiFe-($SO_3^{2-}$)-LDH and NiFe-($S_2O_8^{2-}$)-LDH are almost unchanged after the OER process (Fig. S15 in the ESM). This further demonstrates the long-term stability of the intercalated anions and metal sites. These results are also consistent with our previous report [45].

### 2.6 Simulation results

DFT+U calculations and Bader charge analysis were carried out to further investigate the effects of charge transfer from anions to metal sites in the NiFe-LDHs [63]. The lattice parameters of the different NiFe-LDHs are shown in Table S5 in the ESM, whereas the structures of NiFe-($Cl^-$)-LDH, NiFe-($ClO^-$)-LDH, NiFe-($SO_3^{2-}$)-LDH, and NiFe-($HPO_3^{2-}$)-LDH, selected as representative LDHs, are illustrated in Fig. S16 in the ESM.

Figure 8 displays the binding energies measured from the XPS analysis and the calculated Bader charges of Ni and Fe atoms as a function of the experimentally measured onset potential for different anion-intercalated NiFe-LDHs. We note that a large amount of charge is transferred to the metal sites in the case of intercalated anions with low standard redox potential, such

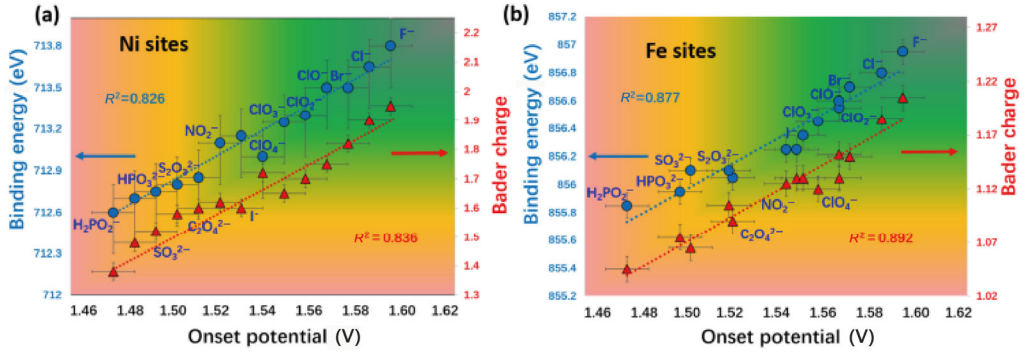


**Figure 8** Binding energy and Bader charge of (a) Ni and (b) Fe sites as a function of the experimentally measured onset potential in as-prepared LDHs (●: Binding energy; ▲: Bader charge).

as $H_2PO_2^-$. As a result, the Ni and Fe oxidation states change and their binding energies decrease. These changes lead to highly active Ni and Fe sites, with lower onset potential and improved OER activity. These results further support the experimental observations and confirm that the valence state the metal sites and the OER activity of the NiFe-LDHs catalysts can be modified by varying the intercalated anions. In the case of the NiFe-based catalysts used in the OER process, the issue of which element (Ni or Fe) is the actual active species has been debated for a long time, and both sides have been supported by experiments and calculations [35, 64]. Based on Fig. 8, the onset potential, binding energy, and Bader charge of Fe show a better correlation compared with those of Ni, implying that Fe plays a more important role than Ni in the OER. Upon intercalation by anions with strong reducing ability, the electron-rich Fe in NiFe-LDHs can be oxidized to higher valence states more easily; the high-valence states of Fe also possess better stability, thus boosting the OER catalytic performance of the NiFe-LDHs.

## 3 Conclusions

In summary, 16 anions with different reducing ability were intercalated in the interlayers of NiFe-LDHs by a co-precipitation process. The performances of the intercalated NiFe-(X)-LDHs as electrocatalysts for the oxygen evolution reaction were then investigated. Based on onset potential, Tafel slope, and OER current density measurements, NiFe-($H_2PO_2^-$)-LDHs and NiFe-($F^-$)-LDHs showed the best and worst OER catalytic activity, respectively. XPS analysis and DFT+U calculations revealed a linear relationship between reducing ability of intercalated anions, electron density of Ni and Fe sites, and OER activity of the corresponding NiFe-LDHs. We showed that intercalated anions with strong reducing ability modify the electronic structure of surface metal sites and significantly improve the performance of the NiFe-LDHs. Compared with Ni, Fe may play a more crucial role in the OER process; however, further work is required to determine the actual active sites. This study not only points to $H_2PO^{2-}$-intercalated NiFe-LDHs as cost-effective, highly active, and durable OER electrocatalysts, but also provides a framework to design and synthesize more efficient electrocatalysts for future energy conversion devices.

## Acknowledgements

This work was supported by the National Natural Science Foundation of China (NSFC), the National Key Research and Development Project (Nos. 2016YFF0204402 and 2016YFC0801302), the Program for Changjiang Scholars, and innovative Research Team in the University, and the Fundamental Research Funds for the Central Universities, and the long term subsidy mechanism from the Ministry of Finance and the Ministry of Education of China. S. S. gratefully acknowledges Villum Foundation.

**Electronic Supplementary Material**: Supplementary material (preparation methods, characterization details, polarization curves, electric double layer capacitance

measurements, potentiostatic stability testing, XPS, lattice parameters) is available in the online version of this article at https://doi.org/10.1007/s12274-017-1750-9.

## References


[1] Wang, H. F.; Tang, C.; Zhang, Q. Towards superior oxygen evolution through graphene barriers between metal substrates and hydroxide catalysts. *J. Mater. Chem. A* **2015**, *3*, 16183–16189.

[2] Cheng, F. Y.; Shen, J.; Peng, B.; Pan, Y. D.; Tao, Z. L.; Chen, J. Rapid room-temperature synthesis of nanocrystalline spinels as oxygen reduction and evolution electrocatalysts. *Nat. Chem.* **2011**, *3*, 79–84.

[3] Han, N.; Zhao, F. P.; Li, Y. G. Ultrathin nickel-iron layered double hydroxide nanosheets intercalated with molybdate anions for electrocatalytic water oxidation. *J. Mater. Chem. A* **2015**, *3*, 16348–16353.

[4] Spöri, C.; Kwan, J. T. H.; Bonakdarpour, A.; Wilkinson, D. P.; Strasser, P. The stability challenges of oxygen evolving catalysts: Towards a common fundamental understanding and mitigation of catalyst degradation. *Angew. Chem., Int. Ed.* **2017**, *56*, 5994–6021.

[5] Zhao, J. W.; Chen, J. L.; Xu, S. M.; Shao, M. F.; Zhang, Q.; Wei, F.; Ma, J.; Wei, M.; Evans, D. G.; Duan, X. Hierarchical NiMn layered double hydroxide/carbon nanotubes architecture with superb energy density for flexible supercapacitors. *Adv. Funct. Mater.* **2014**, *24*, 2938–2946.

[6] Zhao, M. Q.; Zhang, Q.; Huang, J. Q.; Wei, F. Hierarchical nanocomposites derived from nanocarbons and layered double hydroxides-properties, synthesis, and applications. *Adv. Funct. Mater.* **2012**, *22*, 675–694.

[7] Burke, M. S.; Enman, L. J.; Batchellor, A. S.; Zou, S. H.; Boettcher, S. W. Oxygen evolution reaction electrocatalysis on transition metal oxides and (Oxy)hydroxides: Activity trends and design principles. *Chem. Mater.* **2015**, *27*, 7549–7558.

[8] Reier, T.; Nong, H. N.; Teschner, D.; Schlögl, R.; Strasser, P. Electrocatalytic oxygen evolution reaction in acidic environments-reaction mechanisms and catalysts. *Adv. Energy Mater.* **2017**, *7*, 1601275.

[9] Dionigi, F.; Strasser, P. NiFe-based (Oxy)hydroxide catalysts for oxygen evolution reaction in non-acidic electrolytes. *Adv. Energy Mater.* **2016**, *6*, 1600621.

[10] Lee, Y.; Suntivich, J.; May, K. J.; Perry, E. E.; Shao-Horn, Y. Synthesis and activities of rutile $IrO_2$ and $RuO_2$ nanoparticles for oxygen evolution in acid and alkaline solutions. *J. Phys. Chem. Lett.* **2012**, *3*, 399–404.

[11] Diaz-Morales, O.; Raaijman, S.; Kortlever, R.; Kooyman, P. J.; Wezendonk, T.; Gascon, J.; Fu, W. T.; Koper, M. T. M. Iridium-based double perovskites for efficient water oxidation in acid media. *Nat. Commun.* **2016**, *7*, 12363.

[12] Gong, M.; Dai, H. J. A mini review of NiFe-based materials as highly active oxygen evolution reaction electrocatalysts. *Nano Res.* **2015**, *8*, 23–39.

[13] Diaz-Morales, O.; Ledezma-Yanez, I.; Koper, M. T. M.; Calle-Vallejo, F. Guidelines for the rational design of Ni-based double hydroxide electrocatalysts for the oxygen evolution reaction. *ACS Catal.* **2015**, *5*, 5380–5387.

[14] Reier, T.; Oezaslan, M.; Strasser, P. Electrocatalytic oxygen evolution reaction (OER) on Ru, Ir, and Pt catalysts: A comparative study of nanoparticles and bulk materials. *ACS Catal.* **2012**, *2*, 1765–1772.

[15] Cheng, Y.; Jiang, S. P. Advances in electrocatalysts for oxygen evolution reaction of water electrolysis-from metal oxides to carbon nanotubes. *Prog. Nat. Sci.* **2015**, *25*, 545–553.

[16] Tian, G. L.; Zhao, M. Q.; Yu, D. S.; Kong, X. Y.; Huang, J. Q.; Zhang, Q.; Wei, F. Graphene hybrids: Nitrogen-doped graphene/carbon nanotube hybrids: *In situ* formation on bifunctional catalysts and their superior electrocatalytic activity for oxygen evolution/reduction reaction. *Small* **2014**, *10*, 2113.

[17] Takeguchi, T.; Yamanaka, T.; Takahashi, H.; Watanabe, H.; Kuroki, T.; Nakanishi, H.; Orikasa, Y.; Uchimoto, Y.; Takano, H.; Ohguri, N. et al. Layered perovskite oxide: A reversible air electrode for oxygen evolution/reduction in rechargeable metal-air batteries. *J. Am. Chem. Soc.* **2013**, *135*, 11125–11130.

[18] Vojvodic, A.; Nørskov, J. K. Optimizing perovskites for the water-splitting reaction. *Science* **2011**, *334*, 1355–1356.

[19] Grimaud, A.; May, K. J.; Carlton, C. E.; Lee, Y. L.; Risch, M.; Hong, W. T.; Zhou, J. G.; Shao-Horn, Y. Double perovskites as a family of highly active catalysts for oxygen evolution in alkaline solution. *Nat. Commun.* **2013**, *4*, 2439.

[20] Stern, L. A.; Feng, L. G.; Song, F.; Hu, X. L. $Ni_2P$ as a Janus catalyst for water splitting: The oxygen evolution activity of $Ni_2P$ nanoparticles. *Energy Environ. Sci.* **2015**, *8*, 2347–2351.

[21] Chemelewski, W. D.; Lee, H. C.; Lin, J. F.; Bard, A. J.; Mullins, C. B. Amorphous FeOOH oxygen evolution reaction catalyst for photoelectrochemical water splitting. *J. Am. Chem. Soc.* **2014**, *136*, 2843–2850.

[22] Rosen, J.; Hutchings, G. S.; Jiao, F. Ordered mesoporous cobalt oxide as highly efficient oxygen evolution catalyst. *J. Am. Chem. Soc.* **2013**, *135*, 4516–4521.

[23] Jahan, M.; Liu, Z. L.; Loh, K. P. A graphene oxide and

copper-centered metal organic framework composite as a tri-functional catalyst for HER, OER, and ORR. *Adv. Funct. Mater.* **2013**, *23*, 5363–5372.

[24] Suntivich, J.; May, K. J.; Gasteiger, H. A.; Goodenough, J. B.; Shao-Horn, Y. A perovskite oxide optimized for oxygen evolution catalysis from molecular orbital principles. *Science* **2011**, *334*, 1383–1385.

[25] Galizzioli, D.; Tantardini, F.; Trasatti, S. Ruthenium dioxide: A new electrode material. I. Behaviour in acid solutions of inert electrolytes. *J. Appl. Electrochem.* **1974**, *4*, 57–67.

[26] Zhu, X. L.; Tang, C.; Wang, H. F.; Zhang, Q.; Yang, C. H.; Wei, F. Dual-sized NiFe layered double hydroxides *in situ* grown on oxygen-decorated self-dispersal nanocarbon as enhanced water oxidation catalysts. *J. Mater. Chem. A* **2015**, *3*, 24540–24546.

[27] Long, X.; Li, J. K.; Xiao, S.; Yan, K. Y.; Wang, Z. L.; Chen, H. N.; Yang, S. H. A strongly coupled graphene and FeNi double hydroxide hybrid as an excellent electrocatalyst for the oxygen evolution reaction. *Angew. Chem., Int. Ed.* **2014**, *53*, 7584–7588.

[28] Long, X.; Wang, Z. L.; Xiao, S.; An, Y. M.; Yang, S. H. Transition metal based layered double hydroxides tailored for energy conversion and storage. *Mater. Today* **2016**, *19*, 213–226.

[29] Gong, M.; Li, Y. G.; Wang, H. L.; Liang, Y. Y.; Wu, J. Z.; Zhou, J. G.; Wang, J.; Regier, T.; Wei, F.; Dai, H. J. An advanced Ni-Fe layered double hydroxide electrocatalyst for water oxidation. *J. Am. Chem. Soc.* **2013**, *135*, 8452–8455.

[30] Burke, M. S.; Zou, S. H.; Enman, L. J.; Kellon, J. E.; Gabor, C. A.; Pledger, E.; Boettcher, S. W. Revised oxygen evolution reaction activity trends for first-row transition-metal (Oxy)hydroxides in alkaline media. *J. Phys. Chem. Lett.* **2015**, *6*, 3737–3742.

[31] Song, F.; Hu, X. L. Ultrathin cobalt-manganese layered double hydroxide is an efficient oxygen evolution catalyst. *J. Am. Chem. Soc.* **2014**, *136*, 16481–16484.

[32] Zhao, Y. F.; Wei, M.; Lu, J.; Wang, Z. L.; Duan, X. Biotemplated hierarchical nanostructure of layered double hydroxides with improved photocatalysis performance. *ACS Nano* **2009**, *3*, 4009–4016.

[33] Yao, H. B.; Tan, Z. H.; Fang, H. Y.; Yu, S. H. Artificial nacre-like bionanocomposite films from the self-assembly of chitosan-montmorillonite hybrid building blocks. *Angew. Chem., Int. Ed.* **2010**, *49*, 10127–10131.

[34] Han, Y. F.; Liu, Z. H.; Yang, Z. P.; Wang, Z. L.; Tang, X. H.; Wang, T.; Fan, L. H.; Ooi, K. Preparation of $Ni^{2+}$–$Fe^{3+}$ layered double hydroxide material with high crystallinity and well-defined hexagonal shapes. *Chem. Mater.* **2008**, *20*, 360–363.

[35] Louie, M. W.; Bell, A. T. An investigation of thin-film Ni–Fe oxide catalysts for the electrochemical evolution of oxygen. *J. Am. Chem. Soc.* **2013**, *135*, 12329–12337.

[36] Chen, J. Y. C.; Miller, J. T.; Gerken, J. B.; Stahl, S. S. Inverse spinel $NiFeAlO_4$ as a highly active oxygen evolution electrocatalyst: Promotion of activity by a redox-inert metal ion. *Energy Environ. Sci.* **2014**, *7*, 1382–1386.

[37] Tang, C.; Wang, H. S.; Wang, H. F.; Zhang, Q.; Tian, G. L.; Nie, J. Q.; Wei, F. Spatially confined hybridization of nanometer-sized NiFe hydroxides into nitrogen-doped graphene frameworks leading to superior oxygen evolution reactivity. *Adv. Mater.* **2015**, *27*, 4516–4522.

[38] Chen, S.; Duan, J. J.; Jaroniec, M.; Qiao, S. Z. Three-dimensional N-doped graphene hydrogel/NiCo double hydroxide electrocatalysts for highly efficient oxygen evolution. *Angew. Chem., Int. Ed.* **2013**, *52*, 13567–13570.

[39] Ma, W.; Ma, R. Z.; Wang, C. X.; Liang, J. B.; Liu, X. H.; Zhou, K. C.; Sasaki, T. A superlattice of alternately stacked Ni-Fe hydroxide nanosheets and graphene for efficient splitting of water. *ACS Nano* **2015**, *9*, 1977–1984.

[40] Song, F.; Hu, X. L. Exfoliation of layered double hydroxides for enhanced oxygen evolution catalysis. *Nat. Commun.* **2014**, *5*, 4477.

[41] Wang, L.; Wang, D.; Dong, X. Y.; Zhang, Z. J.; Pei, X. F.; Chen, X. J.; Chen, B.; Jin, J. Layered assembly of graphene oxide and Co-Al layered double hydroxide nanosheets as electrode materials for supercapacitors. *Chem. Commun.* **2011**, *47*, 3556–3558.

[42] Oliver-Tolentino, M. A.; Vázquez-Samperio, J.; Manzo-Robledo, A.; de Guadalupe González-Huerta, R.; Flores-Moreno, J. L.; Ramírez-Rosales, D.; Guzmán-Vargas, A. An approach to understanding the electrocatalytic activity enhancement by superexchange interaction toward OER in alkaline media of Ni–Fe LDH. *J. Phys. Chem. C* **2014**, *118*, 22432–22438.

[43] Wang, Q.; O'Hare, D. Recent advances in the synthesis and application of layered double hydroxide (LDH) nanosheets. *Chem. Rev.* **2012**, *112*, 4124–4155.

[44] Hunter, B. M.; Hieringer, W.; Winkler, J. R.; Gray, H. B.; Müller, A. M. Effect of interlayer anions on [NiFe]-LDH nanosheet water oxidation activity. *Energy Environ. Sci.* **2016**, *9*, 1734–1743.

[45] Luo, M.; Cai, Z.; Wang, C.; Bi, Y. M.; Qian, L.; Hao, Y. C.; Li, L.; Kuang, Y.; Li, Y. P.; Lei, X. D. et al. Phosphorus oxoanion-intercalated layered double hydroxides for high-performance oxygen evolution. *Nano Res.* **2017**, *10*, 1732–1739.

[46] Brandán, S. A. Theoretical study of the structure and vibrational spectra of chromyl perchlorate, $CrO_2(ClO_4)_2$. *J. Mol. Struct.*

**2009**, *908*, 19–25.

[47] Hunt, J. M.; Wisherd, M. P.; Bonham, L. C. Infrared absorption spectra of minerals and other inorganic compounds. *Anal. Chem*. **1950**, *22*, 1478–1497.

[48] Miller, F. A.; Wilkins, C. H. Infrared spectra and characteristic frequencies of inorganic ions. *Anal. Chem*. **1952**, *24*, 1253–1294.

[49] Institute of Inorganic Chemistry of Science and Engineering University of Dalian. *Inorganic Chemistry*; 4th ed. Higher Education Press: Beijing, 2001.

[50] Wagman, D. D.; William, H. E.; Parker, V. B.; HandHalow, R.; Schumm, I.; Bailey, S. M.; Churney, K. L.; Nuttall, R. L. The NBS tables of chemical thermodynamic properties: Selected values for inorganic and $C_1$ and $C_2$ organic substances in SI units; American Chemical Society, American Institute of Physics for the National Bureau of Standards: New York, 1982.

[51] Lu, Z. Y.; Qian, L.; Tian, Y.; Li, Y. P.; Sun, X. M.; Duan, X. Ternary NiFeMn layered double hydroxides as highly-efficient oxygen evolution catalysts. *Chem. Commun*. **2016**, *52*, 908–911.

[52] Batchellor, A. S.; Boettcher, S. W. Pulse-electrodeposited Ni–Fe (Oxy)hydroxide oxygen evolution electrocatalysts with high geometric and intrinsic activities at large mass loadings. *ACS Catal*. **2015**, *5*, 6680–6689.

[53] McCrory, C. C. L.; Jung, S.; Ferrer, I. M.; Chatman, S. M.; Peters, J. C.; Jaramillo, T. F. Benchmarking hydrogen evolving reaction and oxygen evolving reaction electrocatalysts for solar water splitting devices. *J. Am. Chem. Soc*. **2015**, *137*, 4347–4357.

[54] Stevens, M. B.; Enman, L. J.; Batchellor, A. S.; Cosby, M. R.; Vise, A. E.; Trang, C. D. M.; Boettcher, S. W. Measurement techniques for the study of thin film heterogeneous water oxidation electrocatalysts. *Chem. Mater*. **2017**, *29*, 120–140.

[55] Laubach, S.; Laubach, S.; Schmidt, P. C.; Ensling, D.; Schmid, S.; Jaegermann, W.; Thißen, A.; Nikolowski, K.; Ehrenberg, H. Changes in the crystal and electronic structure of $LiCoO_2$ and $LiNiO_2$ upon Li intercalation and de-intercalation. *Phys. Chem. Chem. Phys*. **2009**, *11*, 3278–3289.

[56] Lu, Z. Y.; Wang, H. T.; Kong, D. S.; Yan, K.; Hsu, P. C.; Zheng, G. Y.; Yao, H. B.; Liang, Z.; Sun, X. M.; Cui, Y. Electrochemical tuning of layered lithium transition metal oxides for improvement of oxygen evolution reaction. *Nat. Commun*. **2014**, *5*, 4345.

[57] Rossmeisl, J.; Dimitrievski, K.; Siegbahn, P.; Nørskov, J. K. Comparing electrochemical and biological water splitting. *J. Phys. Chem. C* **2007**, *111*, 18821–18823.

[58] Valdés, Á.; Qu, Z. W.; Kroes, G. J.; Rossmeisl, J.; Nørskov, J. K. Oxidation and photo-oxidation of water on $TiO_2$ surface. *J. Phys. Chem. C* **2008**, *112*, 9872–9879.

[59] Yeo, B. S.; Bell, A. T. Enhanced activity of gold-supported cobalt oxide for the electrochemical evolution of oxygen. *J. Am. Chem. Soc*. **2011**, *133*, 5587–5593.

[60] Lu, X. Y.; Zhao, C. Electrodeposition of hierarchically structured three-dimensional nickel-iron electrodes for efficient oxygen evolution at high current densities. *Nat. Commun*. **2015**, *6*, 6616.

[61] Trotochaud, L.; Young, S. L.; Ranney, J. K.; Boettcher, S. W. Nickel-iron oxyhydroxide oxygen-evolution electrocatalysts: The role of intentional and incidental iron incorporation. *J. Am. Chem. Soc*. **2014**, *136*, 6744–6753.

[62] Friebel, D.; Louie, M. W.; Bajdich, M.; Sanwald, K. E.; Cai, Y.; Wise, A. M.; Cheng, M. J.; Sokaras, D.; Weng, T. C.; Alonso-Mori, R. et al. Identification of highly active Fe sites in (Ni, Fe)OOH for electrocatalytic water splitting. *J. Am. Chem. Soc*. **2015**, *137*, 1305–1313.

[63] Liao, P. L.; Keith, J. A.; Carter, E. A. Water oxidation on pure and doped hematite (0001) surfaces: Prediction of Co and Ni as effective dopants for electrocatalysis. *J. Am. Chem. Soc*. **2012**, *134*, 13296–13309.

[64] Lu, Z. Y.; Xu, W. W.; Zhu, W.; Yang, Q.; Lei, X. D.; Liu, J. F.; Li, Y. P.; Sun, X. M.; Duan, X. Three-dimensional NiFe layered double hydroxide film for high-efficiency oxygen evolution reaction. *Chem. Commun*. **2014**, *50*, 6479–6482.